JGR Planets

RESEARCH ARTICLE
10.1029/2022JE007513

Key Points:

- Anomalous bright basal reflections have been detected by MARSIS at Ultimi Scopuli, Mars
- Dielectric measurements of wet clays at low temperature show that they cannot generate strong basal reflections
- Reliable measurements of dielectric behavior of planetary analogs require a careful control of the temperature inside the sample

Correspondence to:
E. Mattei,
elisabetta.mattei@uniroma3.it

Citation:
Cosciotti, B., Mattei, E., Brin, A., Lauro, S. E., Stillman, D. E., Cunje, A., et al. (2023). Can clay mimic the high reflectivity of briny water below the Martian SPLD? *Journal of Geophysical Research: Planets*, *128*, e2022JE007513. https://doi.org/10.1029/2022JE007513

Received 9 AUG 2022
Accepted 14 FEB 2023

Author Contributions:
Conceptualization: Elisabetta Mattei, Elena Pettinelli
Data curation: Barbara Cosciotti, Alessandro Brin, Sebastian Emanuel Lauro, David E. Stillman, Alister Cunje, Dylan Hickson
Formal analysis: Sebastian Emanuel Lauro, David E. Stillman, Alister Cunje, Dylan Hickson
Investigation: Barbara Cosciotti, Alessandro Brin
Methodology: Elisabetta Mattei
Software: Sebastian Emanuel Lauro
Supervision: Elena Pettinelli
Validation: Graziella Caprarelli
Visualization: Barbara Cosciotti, Alessandro Brin, Sebastian Emanuel Lauro
Writing – original draft: Barbara Cosciotti, Elisabetta Mattei, Alessandro Brin, Graziella Caprarelli, Elena Pettinelli

Can Clay Mimic the High Reflectivity of Briny Water Below the Martian SPLD?

Barbara Cosciotti[1], Elisabetta Mattei[1], Alessandro Brin[1], Sebastian Emanuel Lauro[1], David E. Stillman[2], Alister Cunje[3], Dylan Hickson[4], Graziella Caprarelli[5], and Elena Pettinelli[1]

[1]Dipartimento di Matematica e Fisica, Roma Tre University, Rome, Italy, [2]Department of Space Studies, Southwest Research Institute, Boulder, CO, USA, [3]Department of Earth and Environmental Sciences, University of Illinois Chicago, Chicago, IL, USA, [4]Center for Wave Phenomena, Colorado School of Mines, Golden, CO, USA, [5]Centre for Astrophysics, Institute for Advanced Engineering and Space Sciences, University of Southern Queensland, Toowomba, QLD, Australia

Abstract It has recently been suggested that clay minerals, which are widespread on the Martian surface, could be the possible source of the basal bright reflections detected by MARSIS at Ultimi Scopuli, instead of briny water. This hypothesis is based on dielectric measurements on a wet Ca-Montorillonite (STx-1b) sample conducted at 230 K, which reported permittivity values (apparent permittivity of 39 at 4 MHz) compatible with the median value of 33 retrieved by MARSIS 4 MHz data inversion in the high reflectivity area. These experimental results are, however, incompatible with well-established dielectric theory and with laboratory measurements on clays, at MARSIS frequency and Martian temperatures, reported in the literature. Here, we replicate the experiment using a setup to precisely control the rate of cooling/warming and the temperature inside and outside the clay sample. We found that the rate of cooling, the position of the temperature sensor and, consequently, the thermal equilibrium between the sample and the sensor play a fundamental role in the reliability of the measurements. Our results indicate that even for a large water content in the clay sample, at 230 K and 4 MHz, the apparent permittivity is only 8.4, dropping to 4.1 at 200 K, ruling out clays as a possible source of the bright reflections detected by MARSIS at the base of the SPLD.

Plain Language Summary The recent discovery of bright basal reflections below the South polar ice cap at Ultimi Scopuli (Mars) by MARSIS has sparked an intense debate on their origin. Because bright radar reflections detected below the ice sheets in Antarctica and Greenland usually indicate the presence of basal water, and based on additional data processing methods, these anomalies were interpreted to be caused by liquid briny water. Recent laboratory measurements questioned this hypothesis and instead suggested that the presence of clay could explain the observed results. According to these measurements, the dielectric properties of wet clay at 230 K (−43°C) mimic the high reflectivity of briny water. Here, we replicate the experiment, making sure to reach thermal equilibrium during each measurement run to guarantee that the temperature is correctly evaluated when the dielectric properties of the sample are measured. This was accomplished using a dedicated setup to precisely control the thermal cycle and to carefully check the internal and external temperatures of the wet clay sample. Our experimental results clearly show that the dielectric properties of clay at 230 K are incompatible with the observed MARSIS anomalies and thus briny water remains the most plausible explanation for the bright basal reflections detected by MARSIS.

1. Introduction

The search for liquid water below the Martian polar caps is particularly challenging and its presence can only be inferred from geophysical methods. The recent evidence of liquid brines below the SPLD (South Polar Layer Deposits) at Ultimi Scopuli, is indeed based on MARSIS (Mars Advanced Radar for Subsurface and Ionosphere Sounding) radar data inversion, which provided an anomalous high apparent dielectric permittivity value (Mattei et al., 2022; Orosei et al., 2018), interpreted as an indication of ponded water below the ice sheet (Lauro et al., 2021). However, several alternative interpretations have also been proposed (Bierson et al., 2021; Grima et al., 2022; Smith et al., 2021). Among those, it has been suggested that clays, specifically smectites, could be the source of such strong radar reflections. Clay-bearing deposits have been detected on Mars by orbiters (e.g., Bibring et al., 2006; Murchie et al., 2007) and rovers (e.g., Bristow et al., 2018; Clark et al., 2007; Rampe et al., 2020). The visible/near infrared spectrometers Compact Reconnaissance Imaging Spectrometer for Mars

(CRISM), and Observatoire pour la Minéralogie, l'Eau, les Glaces, et l'Activité (OMEGA), identified small and widespread deposits of these minerals between the latitudes 40°S to 40°N in early Noachian to middle Hesperian (4.1–3.3 Ga) terrains (Carter et al., 2013; Ehlmann & Edwards, 2014). Poleward of these latitudes, it is likely that the presence of clay deposits is masked by a thin sedimentary layer formed by the progressive desiccation of ground-ice rich regolith and polar processes (Kreslavsky & Head, 2002; Mustard et al., 2001), although no direct evidence of clay outcrops in the terrains around the SPLD has been reported thus far (e.g., Ehlmann et al., 2011). The susceptibility of these minerals to fragmentation and pulverization suggests, however, that these may be easily lifted and spread globally by Martian winds. It is thus reasonable to speculate that clay minerals may have concentrated in the top regolith layer at the base of the SPLD (Smith et al., 2021).

Clay minerals on Mars include mainly Fe/Mg smectite (e.g., nontronite, saponite) observed at 75% of analyzed sites (Ehlmann et al., 2013), chlorite (often found in impact crater deposits) and Al-bearing phyllosilicates (kaolinite, montmorillonite and beidellite), with minor amounts of illite, vermiculite and poorly crystalline clays (such as: allophane, imogolite and ferrihydrite) (Carter et al., 2013; Ehlmann et al., 2013; Rampe et al., 2012). Smectites are a group of highly expandable phyllosilicates that form using diagenetic or hydrothermal processes involving isochemical changes of precursor materials or by direct deposition from colloids or solutions (Odom, 1984). Structurally, smectites are 2:1 phyllosilicates, in which one octahedral sheet is sandwiched between two silica tetrahedra sheets. The octahedral sites are occupied by Al^{3+} (with Fe^{3+} substitutions) in dioctahedral smectites, and by Mg^{2+} and Fe^{2+} in trioctahedral smectites (Odom, 1984). The interlayer space between two 2:1 layers is partially occupied by larger cations (required to balance charges, typically Na^{+} and Ca^{2+}) surrounded by water molecules that form hydration shells around the cations. Depending on the quantity of interlayer water adsorbed, which in turn depends on the type of cation present and the amount of water available, the basal spacing varies from a minimum of 9.6 Å (fully collapsed state) to a maximum of 19 Å in Ca-montmorillonite (one of the most common varieties on Earth) (Odom, 1984). The variability of interlayer cations and quantity of interlayer water adsorbed causes high disorder in the stacking of smectites, which are thus particularly friable and prone to fragment into very fine particulate.

The dielectric properties of clays have been investigated in a wide variety of studies, from the behavior of vermiculite-confined water (Bergman & Swenson, 2000) to industrial applications (Cadène et al., 2006) and radioactive waste disposal (Meunier et al., 1998), to name a few. Their dielectric behavior is controlled by their structure and the way water molecules and ions electrically interact with the crystal lattice (e.g., Mattei et al., 2022 and references therein). Below the terrestrial ice sheets, clays could be a potential source of bright radar reflections (Tulaczyk & Foley, 2020) because at such a relatively high temperature (~268 K) the water inside the clays remains liquid. This is probably not true for the base of the SPLD where the temperature is predicted to be much lower (~200 K, Orosei et al., 2018; Lauro et al., 2022). Under these conditions, any clay-rich deposit present at the base of the ice should be completely frozen, regardless of its water content, and from a dielectric point of view would behave like a dry material (Mattei et al., 2022; Stillman & Grimm, 2011). In fact, it is well known that the dielectric response of clays is strongly frequency- and temperature-dependent (e.g., Lorek & Wagner, 2013; Olhoeft, 1981). For example, in the MHz range typical of radar sounders, wet clay complex dielectric permittivity values decrease abruptly at low temperatures relative to those measured at standard temperature (Mattei et al., 2022). Therefore, a large part of the experiments reported in the literature, which are usually performed at standard temperatures (about 300 K), are not useful to understand the dielectric response of clays below the ice at Martian temperatures and would not be further discussed in this work.

Recently, Mattei et al. (2022) reviewed the literature relevant to the dielectric behavior of clays at very low temperature (around 200 K), highlighting that neither theoretical nor experimental data support the hypothesis that frozen clays have a large complex dielectric permittivity consistent with the subglacial basal reflections detected by MARSIS at Ultimi Scopuli. Smith et al. (2021), however, reported anomalously large complex dielectric permittivity values for a smectite sample, mixed with a large amount of water, at ~230 K. Because those values contrast significantly with the results reported at MARSIS frequency by other authors (e.g., Stillman et al., 2022), we replicated Smith et al.'s (2021) experiments in an effort to understand the origin of such discrepancy. We used the same type of clay (STx-1b) and followed the same general approach described by those authors, running experiments over the frequency interval 1–100 MHz and at temperatures between 200 and 290 K. The experimental setup was designed to accurately control the temperature ramping and to monitor the temperature inside and outside the clay sample. Our results support and reinforce accepted theo-

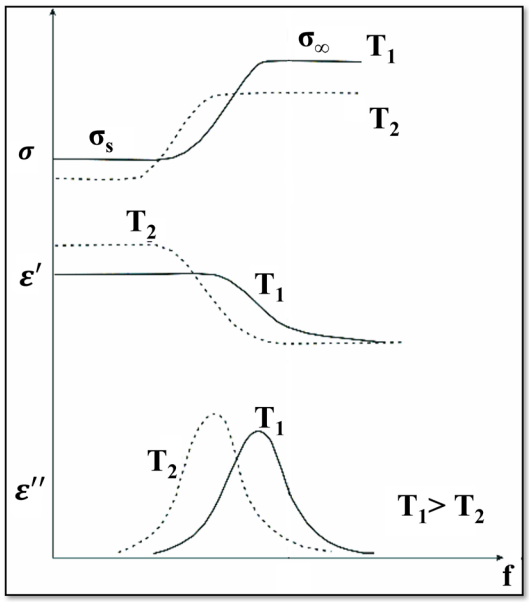

Figure 1. Schematic representation of the effect of temperature on the dielectric parameters of a material having a single relaxation. T_1 and T_2 are two different temperatures, and σ_∞ is the high frequency limit of electrical conductivity.

retical knowledge of the dielectric behavior of clays and propose a possible explanation for the reasons behind the high permittivity values reported by Smith et al. (2021).

2. Materials and Methods

2.1. Clay Dielectric Properties

Dielectric properties of materials are described by the complex dielectric permittivity:

$$\varepsilon = \varepsilon' - j\varepsilon'' \tag{1}$$

where ε' is the real part of the permittivity and indicates the energy storage in the material, and ε'':

$$\varepsilon'' = \varepsilon''_p + \frac{\sigma_S}{2\pi f \varepsilon_0} \tag{2}$$

takes into account the energy dissipation due to polarization losses and migration of free charge carriers (conduction). In Equation 2 $\varepsilon_0 = 8.85 \cdot 10^{-12} F/m$ is the dielectric permittivity in a vacuum, σ_S is the static conductivity, ε''_p the imaginary term due to polarization and f the frequency. From Equation 2 we can also define the frequency-dependent conductivity as follows:

$$\sigma = \sigma_S + 2\pi f \varepsilon_0 \varepsilon''_P \tag{3}$$

The dielectric behavior of clays, in particular smectites, can be very complex (e.g., Cadène et al., 2006; Lorek & Wagner, 2013; Sposito & Prost, 1982) due to the different forms of water: *interlayer water*, *electrostatic double layer water* and *free porewater* (see Wersin et al., 2004 for details). These three types of water respond differently to frequency and temperature, and the real and imaginary parts combine in the overall spectra in a very complicated manner (e.g., Lorek & Wagner, 2013). In general, at each specific frequency, the lower the temperature, the lower the complex dielectric permittivity due to a shift in the spectra of the dielectric parameters (ε', ε'', and σ) toward lower frequencies. From top to bottom Figure 1 schematically shows the effect of temperature on σ, ε', and ε'', considering a single relaxation process (Debye-like model). However, it must be highlighted that clays can be affected by more than one relaxation (e.g., Maxwell-Wagner, bond water, free water), each following the same general trend with temperature (e.g., Lorek & Wagner, 2013; Vasilyeva et al., 2014).

The dielectric behavior of dry and wet smectites as a function of frequency and temperature has been summarized elsewhere (Mattei et al., 2022) and will not be discussed here; in general, it is expected that at Martian temperatures (~200 K) and MARSIS frequencies (3–5 MHz) all relaxation processes are shifted below 1 kHz (Lorek & Wagner, 2013).

2.2. Sample Preparation and Measurement Procedure

We applied the same frequency domain approach described in Smith et al. (2021), performing dielectric measurements in a transmission line filled with the test material. We used a custom coaxial-cage line (Figure 2a) and measured the scattering parameters of the line, from which the complex dielectric permittivity and magnetic permeability of the material were estimated. Coaxial-cage line characteristics and measurement principle are described in detail in Appendix A.

We first report the measurement results in terms of real and imaginary parts, from which we computed the apparent permittivity ε_{app} (Mattei et al., 2022) as follows:

$$\varepsilon_{app} = \varepsilon_1 \left[\frac{1+|\Gamma_{12}|}{1-|\Gamma_{12}|}\right]^2 = \varepsilon_1 \frac{\varepsilon_1 + |\varepsilon_2| + \sqrt{\varepsilon_1^2 + |\varepsilon_2|^2 - 2\varepsilon_1\varepsilon'_2}}{\varepsilon_1 + |\varepsilon_2| - \sqrt{\varepsilon_1^2 + |\varepsilon_2|^2 - 2\varepsilon_1\varepsilon'_2}} \tag{4}$$

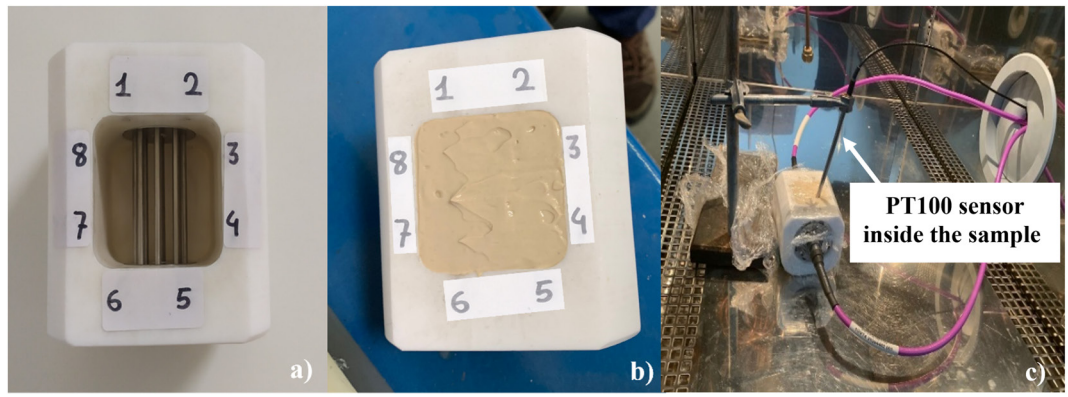

Figure 2. Experimental setup used to perform the dielectric measurements: (a) Coaxial-cage line mounted inside the Teflon cell; (b) Wet STx-1b sample inside the cell before measurements; (c) coaxial cell inside the climatic chamber before starting a measurement run. The PT100 sensor was inserted inside the sample, just above the coaxial-cage.

where $\varepsilon_1 = 3.5$ is the SPLD ice permittivity and ε_2 is the complex permittivity of the material under test, Γ_{12} is the reflection coefficient of a normally impinging plane wave at an interface between two adjacent materials (the SPLD ice and the unknown basal material). The apparent permittivity is a single real quantity that accounts for both polarization and conductive processes and is the physical quantity that MARSIS measures if a material of complex permittivity ε_2 would lay below the SPLD. In Orosei et al. (2018), the median permittivity retrieved by inverting anomalous bright MARSIS data, collected at 4 MHz, is 33. In Mattei et al. (2022), this value was used as a threshold to assess if a given material could be a potential source of the subglacial bright reflections at Ultimi Scopuli.

The sample analyzed in this paper is a Ca-montmorillonite from Texas (Manning formation, Jackson group, Eocene) classified as STx-1b and supplied by The Clay Minerals Society (https://www.clays.org/). The STx-1b clay is a standard used by several authors to run experiments on the dielectric properties of clays (Brown et al., 2004; Canan, 1999; Cunje et al., 2018; Stillman & Grimm, 2011) and has also been used by Smith et al. (2021). The baseline characterization, including chemical composition and X-ray spectroscopy, can be found in Castellini et al. (2017). Based on quantitative x-ray powder diffraction (XRPD) analysis, the sample was composed of montmorillonite (73%), cristobalite (12.8%), tridymite (11.6%), amorphous carbonates and sulfates (2%), and quartz (0.12%). We measured the liquid limit (LL = 118) and the plastic limit (PL = 55) of the STx-1b sample by the Casagrande cup device and the rolling test (ASTM D-18, 2010), respectively, finding values slightly different from previous measurements (LL = 142; PL = 44) performed on a similar sample by Kozlowski and Nartowska (2013). We also measured the grain density of the dry clay sample using a Gas (He) Displacement Pycnometry System (*Micromeritics Accupyc 1340*), obtaining a value 2.267 ± 0.001 g/cm^3 in agreement with that reported in the datasheet (2.2 g/cm^3) of The Clay Minerals Society. We first dried the clay at 105°C for 24 hr in a vacuum oven, then poured the clay in the coaxial cell without compaction, obtaining a bulk density of 0.52 g/cm^3 (77% porosity); finally, we performed the electromagnetic measurements. A second clay sample was dried using the same procedure, transferred to an aluminum container, and distilled water was slowly added while mixing with a spatula to produce a lump-free homogeneous and smooth paste. The coaxial cell was filled with this paste (Figure 2b) and vibrated with a mechanical plate for 20 min to prevent air bubbles from being trapped in the sample and to eliminate any excess liquid water forming at the surface. From an aliquot of the sample, we measured final water content of 128% (expressed as the mass of water to the mass of solids ratio) for a bulk density of 1.27 g/cm^3 estimated from the sample inside the cell.

We performed electromagnetic measurements on the dry and wet samples over the temperature range 200–290 K using a climatic chamber (DY340C - *ACS Angelantoni*) to accurately control the cooling/warming phases of the thermal cycle and thus the temperature inside and outside the sample. A PT100 (Platinum thermoresistance) sensor connected to a multimeter (*Keithley 2700*) was inserted in the sample above the coaxial cage to prevent electromagnetic interference (Figure 2c). Two other PT100 sensors, built into the lateral walls of the chamber, were monitored via the chamber software. The climatic chamber performs thermal cycles at user-defined rates: we first chose a very slow rate, 0.04 K/min, to ensure that both the dry and wet samples reached thermal

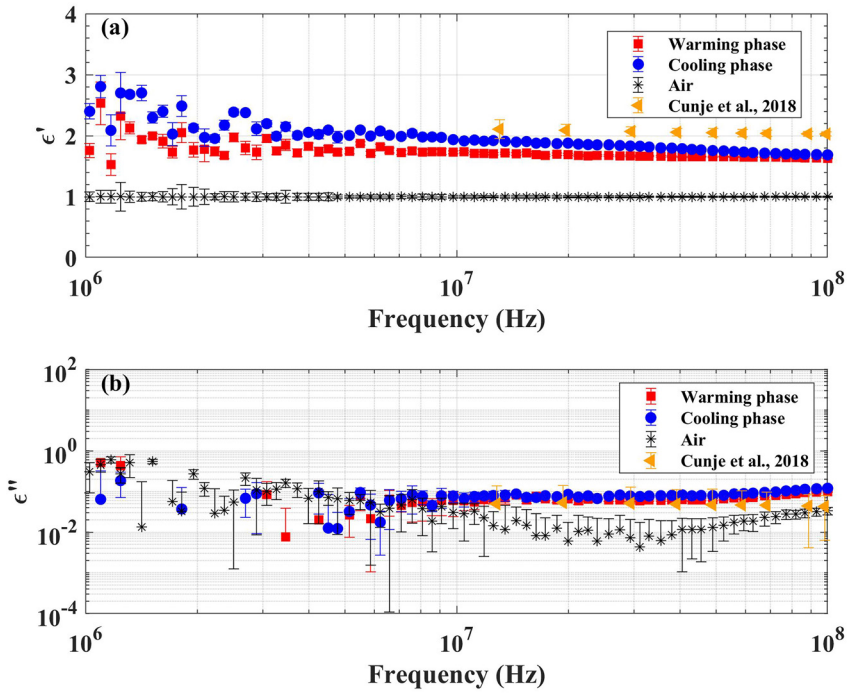

Figure 3. Results from the slow temperature ramping tests conducted on the dry STx-1b dry sample, showing the (a) real and (b) imaginary parts of the relative dielectric permittivity as a function of frequency at 220 K. Uncertainties have been calculated according to Brin et al. (2022).

equilibrium before each dielectric measurement. We then performed the measurements on the wet sample at a faster rate (1 K/min) to study how this experimental parameter affects bulk internal temperature during the measurement procedure. Temperature and electromagnetic data were recorded every 5 min. The reported chamber temperature represents the average of the two chamber-wall sensors described above.

In addition, because in the results we compare our measurements with those performed at 220 K on the same type of clay (STx-1b) by Cunje et al. (2018), which employed the same VNA and similar 15 cm coaxial cell used by Smith et al. (2021) but applying a different cooling approach, we describe their methodology in Appendix B.

3. Results

3.1. Slow Thermal Cycle—Internal Sensor

The real and imaginary parts of the relative dielectric permittivity as a function of frequency are reported in Figure 3 for the dry clay sample measured at 220 K. Complex dielectric permittivity values of an ideal loss-free material (air) obtained by measuring the empty coaxial cell during a similar thermal cycle (same rate) are also shown in the plots and represent the lower limits of the experimental setup. The trend of the data versus frequency is rather regular and no significant dispersion is present, as expected for a loose (porous and air filled) dry material (Olhoeft, 1981). Moreover, no substantial difference is evident in the two phases (cooling/warming) of the cycle. The real part varies from 2.4 to 1.7 moving from low to high frequencies, whereas the imaginary part is only measurable above 10^7 Hz, where it remains almost constant at about 7×10^{-2}. Complex magnetic permeability measurements provide a constant value with a frequency of the order of 1.00 ± 0.01 for the real part and 10^{-2} for the imaginary part, suggesting that the clay is not magnetic. Figure 3 also shows, for comparison, a new set of data from measurements by Cunje et al. (2018) on the STx-1b dry clay at 220 K, performed inserting coaxial line and cables in a So-Low Ultra-Low freezer to reach thermal equilibrium before measurements (Appendix B). The reported values start at 10^7 Hz; the real part is slightly higher, probably due to the larger bulk density (0.79 g/cm^3) of the sample, whereas the imaginary parts are comparable and only diverge slightly at higher frequencies.

The results of the wet clay (128 wt% of water) measurements at $T = 230$ K are illustrated in Figure 4, plotted as a function of frequency. No significant difference is evident in the data from the cooling and warming phases

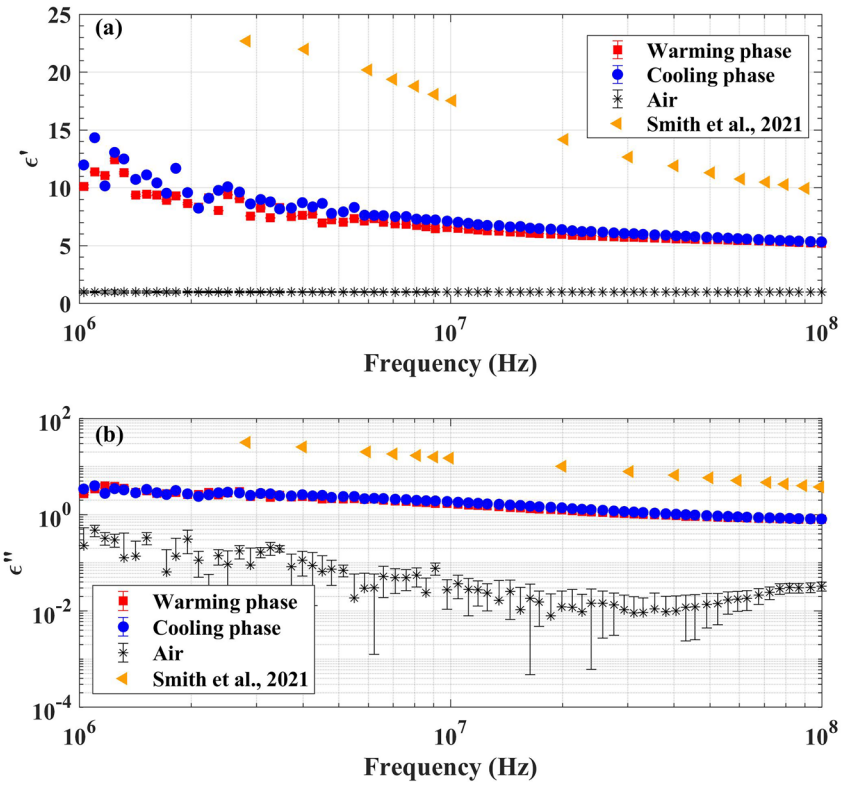

Figure 4. Results from the slow temperature ramping tests conducted on the wet STx-1b sample, showing real (a) and imaginary (b) parts of the relative dielectric permittivity as a function of frequency at 230 K. Uncertainties have been calculated according to Brin et al. (2022).

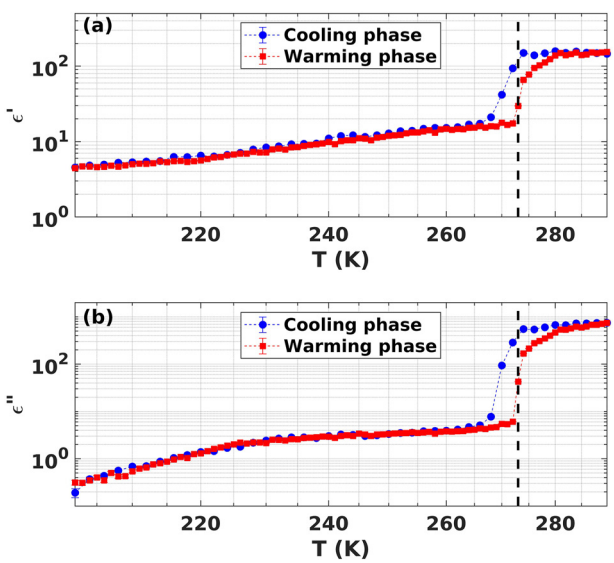

Figure 5. (a) Real and (b) imaginary parts of the relative dielectric permittivity for the wet STx-1b sample at 4 MHz as a function of the temperature measured with the internal sensor. Uncertainties have been calculated according to Brin et al. (2022) but are not visible in the plots as they are smaller than the symbols. The abrupt drop in permittivity values is due to water/ice phase transition; black dashed lines indicate the temperature at which the transition phase of pure water occurs.

of the cycle. The real part shows a typical dispersive behavior, with values ranging from 14 (at 1 MHz) to 5 (100 MHz), while the imaginary part linearly decreases from ∼4 (at 1 MHz) to 0.8 (100 MHz). For comparison, we have also plotted the (digitized) data collected on the "fully hydrated" STx-1b sample at the same temperature (230 K) described by Smith et al. (2021). These values have a real part that is on average 2x that presented here and an imaginary part that is an order of magnitude larger.

To focus on the MARSIS frequency, Figure 5 reports the real and imaginary parts of the dielectric permittivity acquired at 4 MHz as a function of the temperature measured inside the sample. In these plots, both parameters show an abrupt drop around 270 K, due to the water/ice phase transition, followed by a monotonic decrease down to 225 K and then a slight slope change to the lowest measured temperature of 200 K. Importantly, the phase transition occurs at a lower temperature for the cooling phase of the thermal cycle, probably due to water supercooling before freezing, and/or to differences in heat latent release/absorption; other than this difference, data from the two phases of the cycle are essentially superimposed. This high level of reproducibility during warming and cooling cycles suggests that, excluding the temperature interval around the phase transition, the slow cycle allows to reach the thermal equilibrium necessary to accurately measure the complex dielectric permittivity.

The data presented in Figure 5 have been used to compute the apparent permittivity at 4 MHz, shown in Figure 6 as a function of temperature. The general trend is very similar to the values reported by Mattei et al. (2022)

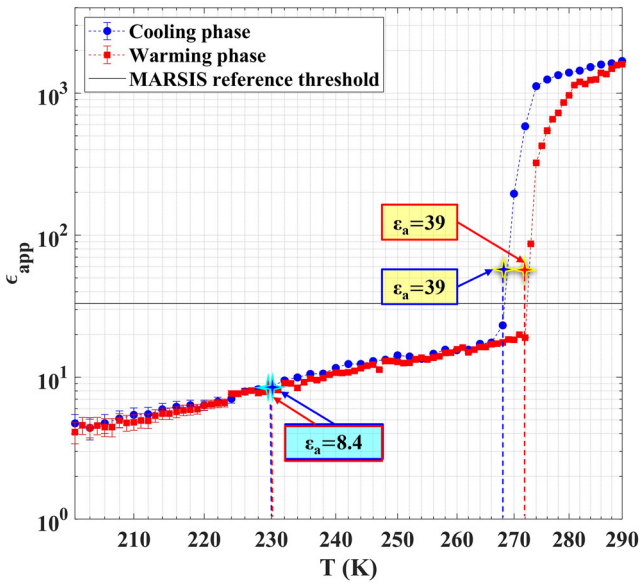

Figure 6. Apparent permittivity of the wet Stx-1b sample measured at 4 MHz as a function of temperature (internal sensor) during the slow temperature ramp. Note that the apparent permittivity value (39) computed from Smith et al.'s (2021) data correspond to temperature around 270 K, suggesting that the sample still contains a remarkable amount of liquid water. The apparent permittivity at 230 K is 8.4.

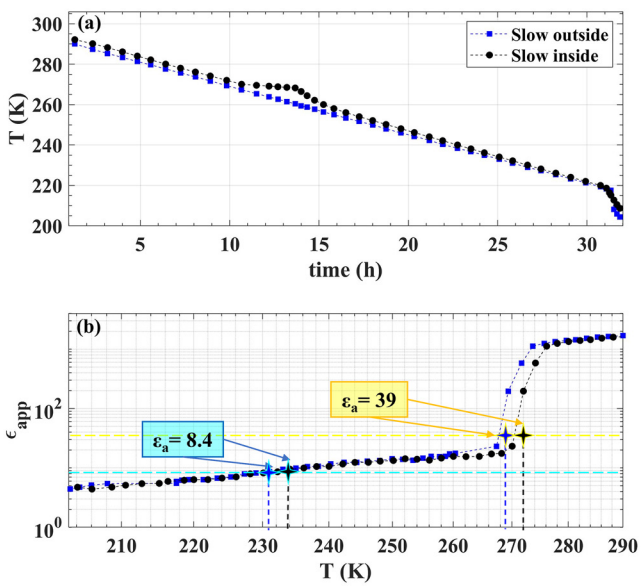

Figure 7. Temperature and apparent permittivity measured during the cooling phase of the slow cycle: (a) Temperature of the internal and external sensors as a function of time; and (b) apparent permittivity as a function of temperature. Black dots indicate the temperature measured by the sensor inside the sample and blue dots by the sensor outside the sample. In (a), the bump in the temperature plot of the internal sensor indicates the water/ice transition phase. Note that in the slow cycle, after about 30 hr of cooling (below 220 K), the temperature rate appears to change; however, such change is not present during the warming phase. In any case, this variation did not affect our results.

for a set of clay sediments with different water contents. In that work, the water contents were given as the ratio between the mass of water and the total mass of the wet sample. If we apply the same formulation, then the wet STx-1b has 56 wt% water. The plot in Figure 6 also shows that at $T < 270$ K the apparent permittivity drops to 20, and then linearly decreases with a decrease in temperature to a value of 8.4 at 230 K (for both cooling and warming stages) through to 4.1 at 200 K. We obtain an apparent permittivity value of 39 at 268 K during cooling, and 273 K for the warming stage of the cycle (Figure 4). These temperatures are ~40 K higher than the temperature (230 K) recorded by Smith et al. (2021) for the same permittivity value.

3.2. Slow Thermal Cycle—Internal Versus External Sensors

Figure 7a shows the variation of temperature inside the coaxial cell and outside the sample (inside the climatic chamber) during the cooling phase of the slow cycle, while Figure 7b shows the apparent permittivity against the temperature measured by the internal and external sensors. The temperature sensor inside the cell records the effect of water freezing in the time interval between 10 and 15 hr which is not measured by the external sensor. The two curves in Figure 7b overlap across the entire investigated interval, except during phase transition. This suggests that during the slow thermal cycle, the internal and the external sensors reach thermal equilibrium. In fact, the internal and external sensors measure almost the same temperature (232 K inside, vs. 230 K outside) for an apparent permittivity of 8.4. The apparent permittivity of 39 is recorded at 270 K by the sensor inside the sample, and 268 K by the outside sensor.

3.3. Fast Thermal Cycle—Internal Versus External Sensors

Figure 8 shows the variation of temperature with time inside and outside the sample, measured during the cooling segment of the fast cycle (a), and the apparent permittivity relative to the temperature measured by the internal and external sensors (b). During the fast thermal cycle, the temperature inside the climatic chamber (measured by the external sensor) reached 200 K, the lowest temperature of the experiment, in only about 2 hr. The sensor inside the cell reaches the same temperature after about 4 hr. This discrepancy between the two sensors dramatically affects the apparent permittivity assigned to each temperature step because the use of the external sensor values shifts the curve to much lower temperatures for a given apparent permittivity compared to the true temperature of the sample (measured by the internal sensor): for example, the apparent permittivity value of 8.4 is reached at 229 K if we consider the internal sensor, whereas the external sensor records a temperature of 202 K. Similarly, an apparent permittivity of 39 is measured at a temperature of 253 K using the inner sensor, and 208 K by the external sensor. It is also important to note that the climatic chamber reaches the minimum temperature (200 K) in approximately 2 hr, when the internal sensor measures ~240 K. Moreover, the chamber remains at 200 K for a long time in a steady-state condition, whereas the temperature inside the sample slowly decay. The apparent permittivity of 8.4 is reached at 229 K, which is very close to the temperature measured for the same value during the slow temperature phase (Figure 7).

4. Discussion

The comparison between the dielectric data collected in this work and those acquired in a different laboratory (Cunje et al., 2018) on a standard clay sample

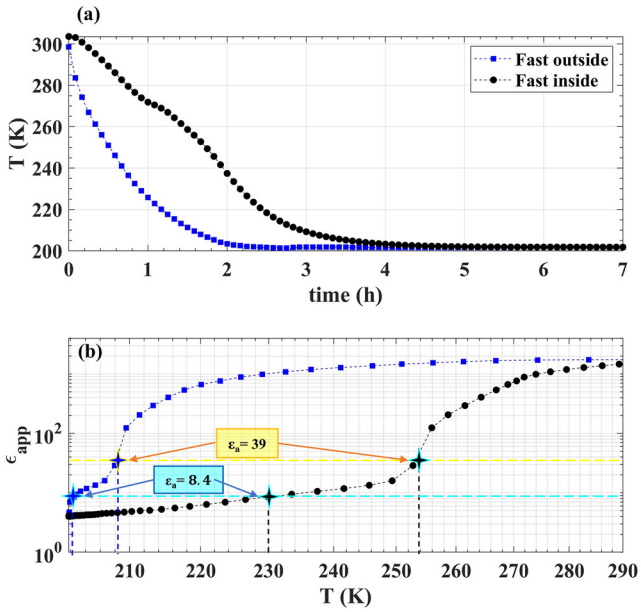

Figure 8. Results measured during the cooling phase of the fast cycle: (a) Temperature of the internal and external sensors as a function of time; and (b) apparent permittivity as a function of temperature. Black dots indicate the temperature measured by the sensor inside the sample and blue dots by the sensor outside the sample. In (a), the bump in the temperature plot of the internal sensor, which lasted about an hour, indicates the water/ice transition phase.

(STx-1b) instills confidence in the reliability of our measurement procedure. In fact, despite the difference in the experimental setup and cooling procedure (via a cooling/warming cycle in our case and in steady-state configuration in Cunje et al. (2018)) once the sample has reached the thermal equilibrium, the retrieved dielectric values are comparable in both experiments (Figure 3). Moreover, our results on the wet STx-1b sample at low temperatures and 4 MHz (Figure 5) are fully consistent with previous measurements obtained using a similar procedure on six smectite- and chlorite-rich sediments having different water contents (cf. Figure 5 in Mattei et al. (2022)). At 230 K, the apparent permittivity of those samples ranged between 6 and 10, close to the value of 8.4 we obtained here. The wet STx-1b sample measured in the present study contains 56 wt% water, which is 2–3 times larger than the water content in the samples measured by Mattei et al. (2022). Thus, the similarity between the apparent permittivity values at 230 K, regardless of the water content, indicates that the water inside the clay is almost totally frozen. At 200 K, which we expect to be within range of the basal temperatures at Ultimi Scopuli, the apparent permittivity drops to 4.1, again in agreement with the values (4–6.4) reported by Mattei et al. (2022), and with other experimental works (e.g., Bittelli et al., 2004; Kułacz & Orzechowski, 2019; Lorek & Wagner, 2013; Moore & Maeno, 1993; Stillman et al., 2010).

The reasons for the large discrepancy between our results and those reported by Smith et al. (2021) could be related to the different sample preparation and experimental procedures followed. First, Smith et al. (2021) indicated that their clay sample was dried at much higher temperatures (200°C) than those recommended using soil-testing guidelines, which may have led to structural modification of the clay. Second, there are various uncertainties related to their description of the sample hydration, such as: (a) the lack of quantitative information on the specific water content of the "fully hydrated sample," despite the fact that highly expandable smectites can be saturated over a range of water contents; (b) the description of clay sample shrinkage after the addition of a large amount of water, in apparent contrast to the well-known swelling property of smectites; and (c) the puzzling fact that the authors declare a bulk density (2.679 g/cm^3) of the "fully hydrated sample" that is higher than the grain density (2.2 g/cm^3). Moreover, we have no way of knowing whether the water content of the "fully hydrated sample" is significantly different from our experiments. Even so, Stillman and Grimm (2011) have measured the complex dielectric permittivity of a similar clay with a larger water content than the one used in the present work (80% in volume of a $CaCl_2$ solution, with eutectic temperature <230 K), from which we computed an apparent permittivity of about 11 at 230 K and 4 MHz. Therefore, even larger water content in the "fully hydrated sample" does not yield the results published by Smith et al. (2021).

Furthermore, Smith et al. (2021) describe how they used conductive tape to attach the thermal sensor to the external part of the metallic coaxial line, then cooling the sample by hosing liquid nitrogen directly on the cell. Our experiment shows that the rate of cooling, the position of the temperature sensorand, consequently, the thermal equilibrium between the sample and the sensor play a fundamental role in the reliability of the measurements. Selecting a slow temperature cycle and ensuring a direct contact between the sensor and the sample is the best procedure to avoid large mistakes in assessing the temperature at which a dielectric measurement has been performed. Under these conditions, the cooling and warming cycles return broadly consistent results, except at around 270 K, during phase transition. It is clear that during fast temperature cycles, the temperatures inside the sample decrease much more slowly than the external temperatures, which may lead to incorrect associations between temperatures and measured values of complex permittivity (Figure 8).

We can conclude that the measurements presented by Smith et al. (2021) attribute dielectric permittivity values to a temperature of 230 K when they actually were collected on a much warmer sample that was not fully solid (frozen). The cooling procedure, involving direct spraying of liquid nitrogen on the coaxial line and positioning the temperature sensor on the external part of the line, did not allow a thermal equilibrium to be reached between the sensor and the sample, thus preventing a correct correspondence between sample temperature and dielectric properties.

5. Conclusions

It has been claimed that low temperature clays, not briny water, could be the source of the bright reflections detected by MARSIS at the base of the SPLD, at Ultimi Scopuli. This interpretation is based on the experiments by Smith et al. (2021), who claimed to have measured a complex permittivity value of 39, higher than the MARSIS reference threshold of 33 computed from radar data at 4 MHz, on a wet smectite sample at 230 K. Such high apparent permittivity at low temperature is, however, inconsistent with dielectric theory and a large body of literature (Mattei et al., 2022, and refs. therein) reporting laboratory measurements obtained on smectites and other type of clays. To investigate the reasons for this discrepancy, we replicated Smith et al.'s (2021) experiments. We found that a clay sample with a large amount of water measured at 230 K and 4 MHz yields an apparent permittivity value of only 8.4, which subsequently drops to 4.1 at 200 K; these values are fully consistent with the well-established dielectric behavior of wet cold clays. Our results suggest poor control of the temperatures inside the experimental clay samples, and rates of cooling probably not conducive to equilibration of the temperatures inside and outside the samples, may have caused Smith et al. (2021) to misread the temperatures at which the dielectric measurements were obtained. Based on our results, which further corroborate previous studies and reinforce knowledge of the dielectric behavior of clays, we conclusively rule out clays as the source of the bright reflections detected by MARSIS at the base of the SPLD.

We emphasize the need to determine the dielectric properties of materials only through slow rate experiments to enhance confidence that the measurements are conducted in conditions as close to thermal equilibrium as possible. Such experiments play a critical role in constraining the geophysical properties of planetary materials detected through satellite missions. To avoid spurious results that may lead to erroneous interpretations, it is thus essential that consistent standards across all laboratories undertaking measurements of dielectric properties of planetary materials are applied.

Appendix A

Transmission lines are commonly used to estimate the electromagnetic properties of materials through the measurements of the scattering parameters (Chen et al., 2004). In our experiment, we used a coaxial line consisting of a Teflon box (having an internal volume of 146.13 cm^3) containing a cylindrical stainless-steel cage formed by a central conductor and eight equally spaced rods (Figures A1 and 2a). The line is connected to a two-port Vector Network Analyzer (Agilent ES5071C) via two cryogenic cables (MegaPhase) capable of maintaining unaltered dielectric characteristics down to 190 K. We computed the complex dielectric permittivity ε and the complex magnetic permeability μ of the clay samples in the frequency range $1 - 100$ MHz from the measured scattering parameters S_{11} and S_{21} using the Nicolson-Ross-Weir algorithm (Nicolson & Ross, 1970; Weir, 1974):

$$K = \frac{S_{11}^2 - S_{21}^2 + 1}{2S_{11}} \tag{A1}$$

$$\Gamma = K \pm \sqrt{K^2 - 1} \tag{A2}$$

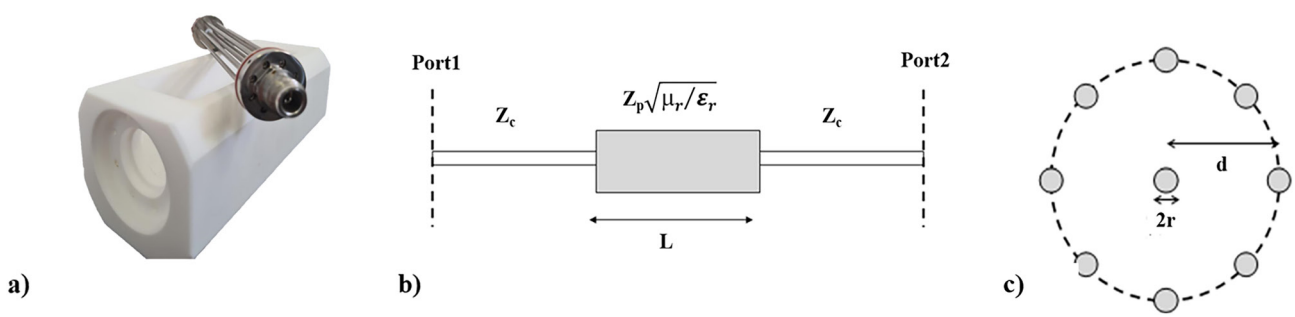

Figure A1. Coaxial-cage and schematic of the transmission line. (a) Photo of the disassembled probe with the eight-rods cage on top the Teflon box; (b) sketch of the transmission line (in light gray) having a characteristic impedance Z_p, connected to the VNA (Port 1 and 2) via cables (in white) having impedance Z_c; (c) cross-section of the coaxial cage, made by eight equally spaced rods (shield) and a central rod (conductor), all having diameter (3.00 ± 0.03) mm and length (50 ± 0.03) mm. The distance between the central conductor and the shield is 9.52 ± 0.03 mm.

$$\Psi = \frac{S_{11} + S_{21} - \Gamma}{1 - (S_{11} + S_{21})\Gamma} \tag{A3}$$

from which the relative complex dielectric permittivity and magnetic permeability can be computed as follows (Mattei et al., 2013):

$$\varepsilon_r = j\frac{c}{2\pi f L}\ln(\Psi)\frac{1-\Gamma}{1+\Gamma}\frac{1}{F_g} \tag{A4}$$

$$\mu_r = j\frac{c}{2\pi f L}\ln(\Psi)\frac{1+\Gamma}{1-\Gamma}F_g \tag{A5}$$

In Equations A4 and A5 $F_g = Z_c/Z_p$ is a geometrical factor accounting for the mismatch between the impedance of the coaxial cable Z_c and the impedance of the coaxial-cage line in air Z_p, L is the electrical length of the coaxial-cage line, f is the frequency and c is the velocity of the electromagnetic wave in a vacuum (see Figure A1b). We estimated the coaxial line F_g and L parameters as a function of temperature and frequency first measuring the probe line empty (air) (Brin et al., 2022), then using reference materials like bidistilled water and pure ethanol, following the procedure described in Mattei et al. (2013). Moreover, before each set of measurements, a calibration procedure was performed using the SOLT standards (Short, Open, Load, Through) HP 85032F calibration kit. This calibration allows to account for the influence of the cables and connectors on the retrieved properties and to properly correct the values of the scattering parameters.

Appendix B

Here, we describe the method of Cunje et al. (2018) given the fact that details of their experimental setup and procedure are not reported in the cited conference abstract. The new data presented in this work is part of a data set measured by Cunje et al. (2018) on the STx-1b dry clay at 220 K, employing the same *Agilent Technologies E5071C* VNA, *Maury Microwave Stability SC-35 Microwave/RF* cables, and the same model *General Radio Company GR900-LZ15* 15 cm 50 Ω coaxial airline/cell used in Smith et al. (2021) work. In Cunje et al. (2018), and for this presented data, STx-1b samples were sieved to <212 μm grain size and dried at 115°C for 48 hr prior to measurement to remove moisture. VNA, coaxial airline, and cable TRM (Thru, Reflection, Match) calibrations were performed, with the calibration and measurement procedures using the experimental setup, software, and the methodology described in Boivin et al. (2018). We direct the reader to Boivin et al. (2018) for further reading but summarize key points here. To adapt the procedure for cold Martian temperature conditions, the VNA calibration measurements and S-parameter measurements of the clay samples were conducted following the general cooling procedure of Stillman and Olhoeft (2008), with the coaxial airline or calibration standards and adaptors, along with a portion of the cables, placed into a *So-Low Ultra-Low* freezer at 220 K. The temperature of the apparatus was monitored with the use of an *OMEGA Temperature Controller* and resistance temperature detector (RTD) fastened to the exterior of the airline. Calibration or S-parameter sample measurements were made only after the apparatus was allowed sufficient time to cool to the desired 220 K measuring temperature, with the RTD temperature sensor displaying consistent readings for at least 20 min to ensure thermal equilibrium. After the calibrations were complete, the airline sample holder was filled with the dried clay sample using the custom funnel, alignment rod, and sieve shaker packing method described in Boivin et al. (2018) and then connected to the VNA via the microwave cables for S-parameter measurements. Consecutive measurements were made after initial S-parameter measurements of the dried and cooled STx-1b clay sample to ensure the consistency of measurement results under the continuous cold conditions, and no variations were observed. Permittivity for the data set reported here was calculated from the S-parameter data using the "*permittivitycalc*" code developed by Boivin and Hickson (2018) based on the Noniterative method in Boughriet et al. (1997), without any normalization of the bulk density.

Data Availability Statement

Data reported in this paper are available at Cosciotti (2023).

Acknowledgments
This work was supported by the Italian Space Agency (ASI) through contract ASI-INAF 2019-21-HH.0. We would like to thank Dr. Antonio Baliva and Dr. Luca Colantuono for help in preparing the clay samples.

References

Bergman, R., & Swenson, J. (2000). Dynamics of supercooled water in confined geometry. *Nature*, *403*(6767), 283–286. https://doi.org/10.1038/35002027

Bibring, J. P., Langevin, Y., Mustard, J. F., Poulet, F., Arvidson, R., Gendrin, A., et al. (2006). Global mineralogical and aqueous Mars history derived from OMEGA/Mars Express data. *Science*, *312*(5772), 400–404. https://doi.org/10.1126/science.11226

Bierson, C. J., Tulaczyk, S., Courville, S. W., & Putzig, N. E. (2021). Strong MARSIS radar reflections from the base of Martian south polar cap may be due to conductive ice or minerals. *Geophysical Research Letters*, *48*(13), e2021GL093880. https://doi.org/10.1029/2021GL093880

Bittelli, M., Flury, M., & Roth, K. (2004). Use of dielectric spectroscopy to estimate ice content in frozen porous media. *Water Resources Research*, *40*(4), W04212. https://doi.org/10.1029/2003WR002343

Boivin, A. L., & Hickson, D. (2018). Permittivitycalc (version v0.5.0) [Dataset]. Zenodo. https://doi.org/10.5281/zenodo.1469776

Boivin, A. L., Hickson, D., Tsai, C., Cunje, A., Ghent, R. R., & Daly, M. G. (2018). Broadband measurements of the complex permittivity of carbonaceous asteroid regolith analog materials. *Journal of Geophysical Research: Planets*, *123*(12), 3088–3104. https://doi.org/10.1029/2018JE005662

Boughriet, A. H., Legrand, C., & Chapoton, A. (1997). Noniterative stable transmission/reflection method for low-loss material complex permittivity determination. *IEEE Transactions on Microwave Theory and Techniques*, *45*(1), 52–57. https://doi.org/10.1109/22.552032

Brin, A., Lauro, S. E., Cosciotti, B., Mattei, E., & Pettinelli, E. (2022). Electromagnetic characterization of a crushed L-chondrite for subsurface radar investigations of solar system bodies. *Icarus*, *374*, 114800. https://doi.org/10.1016/j.icarus.2021.114800

Bristow, T. F., Rampe, E. B., Achilles, C. N., Blake, D. F., Chipera, S. J., Craig, P., et al. (2018). Clay mineral diversity and abundance in sedimentary rocks of Gale crater, Mars. *Science Advances*, *4*(6), eaar3330. https://doi.org/10.1126/sciadv.aar3330

Brown, S. R., Sorenson, J. R., & Brown, T. I. (2004). A laboratory study of the complex electrical resistivity response of soils. In *Symposium on the Application of Geophysics to Engineering and Environmental Problems 2004* (pp. 528–539). Society of Exploration Geophysicists.

Cadène, A., Rotenberg, B., Durand-Vidal, S., Badot, J. C., & Turq, P. (2006). Dielectric spectroscopy as a probe for dynamic properties of compacted smectites. *Physics and Chemistry of the Earth, Parts A/B/C*, *31*(10–14), 505–510. https://doi.org/10.1016/j.pce.2006.04.002

Canan, B. (1999). *Dielectric properties of mixtures of clay-water-organic compounds* (Theses & Dissertations). School of Mines.

Carter, J., Poulet, F., Bibring, J. P., Mangold, N., & Murchie, S. (2013). Hydrous minerals on Mars as seen by the CRISM and OMEGA imaging spectrometers: Updated global view. *Journal of Geophysical Research: Planets*, *118*(4), 831–858. https://doi.org/10.1029/2012JE004145

Castellini, E., Malferrari, D., Bernini, F., Brigatti, M. F., Castro, G. R., Medici, L., et al. (2017). Baseline studies of the clay minerals society source clay montmorillonite STx-1b. *Clays and Clay Minerals*, *65*(4), 220–233. https://doi.org/10.1346/CCMN.2017.064065

Chen, L. F., Ong, C. K., Neo, C. P., Varadan, V. V., & Varadan, V. K. (2004). *Microwave electronics: Measurement and materials characterization*. John Wiley & Sons.

Clark, B. C., III, Arvidson, R. E., Gellert, R., Morris, R. V., Ming, D. W., Richter, L., et al. (2007). Evidence for montmorillonite or its compositional equivalent in Columbia Hills, Mars. *Journal of Geophysical Research*, *112*(E6), E06S01. https://doi.org/10.1029/2006JE002756

Cosciotti, B. (2023). Dataset "Can clay mimic the high reflectivity of briny water below the Martian SPLD?" [Dataset]. Zenodo. https://zenodo.org/record/7525763

Cunje, A. B., Ghent, R. R., Boivin, A., Tsai, C. A., & Hickson, D. (2018). Dielectric properties of Martian regolith analogs and smectite clays. In *Lunar and Planetary Science Conference* (Vol. 2083, p. 1805).

Ehlmann, B. L., Berger, G., Mangold, N., Michalski, J. R., Catling, D. C., Ruff, S. V., et al. (2013). Geochemical consequences of widespread clay mineral formation in Mars' ancient crust. *Space Science Reviews*, *174*(1–4), 329–364. https://doi.org/10.1007/s11214-012-9930-0

Ehlmann, B. L., & Edwards, C. S. (2014). Mineralogy of the Martian surface. *Annual Review of Earth and Planetary Sciences*, *42*(1), 291–315. https://doi.org/10.1146/annurev-earth-060313-055024

Ehlmann, B. L., Mustard, J. F., Murchie, S. L., Bibring, J. P., Meunier, A., Fraeman, A., & Langevin, Y. (2011). Subsurface water and clay mineral formation during the early history of Mars. *Nature*, *479*(7371), 53–60. https://doi.org/10.1038/nature10582

Grima, C., Mouginot, J., Kofman, W., Hérique, A., & Beck, P. (2022). The basal detectability of an ice-covered Mars by MARSIS. *Geophysical Research Letters*, *49*(2), e2021GL096518. https://doi.org/10.1029/2021GL096518

Kozlowski, T., & Nartowska, E. (2013). Unfrozen water content in representative bentonites of different origin subjected to cyclic freezing and thawing. *Vadose Zone Journal*, *12*(1), 1–11. https://doi.org/10.2136/vzj2012.0057

Kreslavsky, M. A., & Head, J. W., III. (2002). Mars: Nature and evolution of young latitude-dependent water-ice-rich mantle. *Geophysical Research Letters*, *29*(15), 14-1–14-4. https://doi.org/10.1029/2002gl015392

Kułacz, K., & Orzechowski, K. (2019). Nontronite and intercalated nontronite as effective and cheap absorbers of electromagnetic radiation. *Dalton Transactions*, *48*(12), 3874–3882. https://doi.org/10.1039/C9DT00132H

Lauro, S. E., Pettinelli, E., Caprarelli, G., Baniamerian, J., Mattei, E., Cosciotti, B., et al. (2022). Using MARSIS signal attenuation to assess the presence of South Polar Layered Deposit subglacial brines. *Nature Communications*, *13*(1), 5686. https://doi.org/10.1038/s41467-022-33389-4

Lauro, S. E., Pettinelli, E., Caprarelli, G., Guallini, L., Rossi, A. P., Mattei, E., et al. (2021). Multiple subglacial water bodies below the south pole of Mars unveiled by new MARSIS data. *Nature Astronomy*, *5*(1), 63–70. https://doi.org/10.1038/s41550-020-1200-6

Lorek, A., & Wagner, N. (2013). Supercooled interfacial water in fine-grained soils probed by dielectric spectroscopy. *The Cryosphere*, *7*(6), 1839–1855. https://doi.org/10.5194/tc-7-1839-2013

Mattei, E., Lauro, S. E., Pettinelli, E., & Vannaroni, G. (2013). Coaxial-cage transmission line for electromagnetic parameters estimation. *IEEE Transactions on Instrumentation and Measurement*, *62*(11), 2938–2942. https://doi.org/10.1109/TIM.2013.2266015

Mattei, E., Pettinelli, E., Lauro, S. E., Stillman, D. E., Cosciotti, B., Marinangeli, L., et al. (2022). Assessing the role of clay and salts on the origin of MARSIS basal bright reflections. *Earth and Planetary Science Letters*, *579*, 117370. https://doi.org/10.1016/j.epsl.2022.117370

Meunier, A., Velde, B., & Griffault, L. (1998). The reactivity of bentonites: A review. An application to clay barrier stability for nuclear waste storage. *Clay Minerals*, *33*(2), 187–196. https://doi.org/10.1180/000985598545462

Moore, J. C., & Maeno, N. (1993). Dielectric properties of frozen clay and silt soils. *Cold Regions Science and Technology*, *21*(3), 265–273. https://doi.org/10.1016/0165-232X(93)90070-O

Murchie, S., Arvidson, R., Bedini, P., Beisser, K., Bibring, J. P., Bishop, J., et al. (2007). Compact reconnaissance imaging spectrometer for Mars (CRISM) on Mars reconnaissance orbiter (MRO). *Journal of Geophysical Research*, *112*(E5), E05S03. https://doi.org/10.1029/2006JE002682

Mustard, J. F., Cooper, C. D., & Rifkin, M. K. (2001). Evidence for recent climate change on Mars from the identification of youthful near-surface ground ice. *Nature*, *412*(6845), 411–414. https://doi.org/10.1038/35086515

Nicolson, A. M., & Ross, G. F. (1970). Measurement of the intrinsic properties of materials by time-domain techniques. *IEEE Transactions on Instrumentation and Measurement*, *19*(4), 377–382. https://doi.org/10.1109/tim.1970.4313932

Odom, I. E. (1984). Smectite clay minerals: Properties and uses. *Philosophical Transactions of the Royal Society of London - Series A: Mathematical and Physical Sciences*, *311*(1517), 391–409. https://doi.org/10.1098/rsta.1984.0036

Olhoeft, G. R. (1981). Electrical properties of rocks. *Physical properties of rocks and minerals* (Vol. 2, pp. 257–297).

Orosei, R., Lauro, S. E., Pettinelli, E., Cicchetti, A., Coradini, M., Cosciotti, B., et al. (2018). Radar evidence of subglacial liquid water on Mars. *Science*, *361*(6401), 490–493. https://doi.org/10.1126/science.aar7268

Rampe, E. B., Blake, D. F., Bristow, T. F., Ming, D. W., Vaniman, D. T., Morris, R. V., et al. (2020). Mineralogy and geochemistry of sedimentary rocks and eolian sediments in Gale crater, Mars: A review after six Earth years of exploration with Curiosity. *Geochemistry*, *80*(2), 125605. https://doi.org/10.1016/j.chemer.2020.125605

Rampe, E. B., Kraft, M. D., Sharp, T. G., Golden, D. C., Ming, D. W., & Christensen, P. R. (2012). Allophane detection on Mars with Thermal Emission Spectrometer data and implications for regional-scale chemical weathering processes. *Geology*, *40*(11), 995–998. https://doi.org/10.1130/G33215.1

Smith, I. B., Lalich, D. E., Rezza, C., Horgan, B. H. N., Whitten, J. L., Nerozzi, S., & Holt, J. W. (2021). A solid interpretation of bright radar reflectors under the Mars south polar ice. *Geophysical Research Letters*, *48*(15), e2021GL093618. https://doi.org/10.1029/2021GL093618

Sposito, G., & Prost, R. (1982). Structure of water adsorbed on smectites. *Chemical Reviews*, *82*(6), 553–573. https://doi.org/10.1021/cr00052a001

Stillman, D., & Olhoeft, G. (2008). Frequency and temperature dependence in electromagnetic properties of Martian analog minerals. *Journal of Geophysical Research*, *113*(E9), E09005. https://doi.org/10.1029/2007JE002977

Stillman, D. E., & Grimm, R. E. (2011). Radar penetrates only the youngest geological units on Mars. *Journal of Geophysical Research*, *116*(E3), E03001. https://doi.org/10.1029/2010JE003661

Stillman, D. E., Grimm, R. E., & Dec, S. F. (2010). Low-frequency electrical properties of ice−silicate mixtures. *The Journal of Physical Chemistry B*, *114*(18), 6065–6073. https://doi.org/10.1021/jp9070778

Stillman, D. E., Pettinelli, E., Lauro, S. E., Mattei, E., Caprarelli, G., Cosciotti, B., et al. (2022). Partially-saturated brines within basal ice or sediments can explain the bright basal reflections in the south polar layered deposits. *Journal of Geophysical Research: Planets*, *127*(10), e2022JE007398. https://doi.org/10.1029/2022je007398

Tulaczyk, S. M., & Foley, N. T. (2020). The role of electrical conductivity in radar wave reflection from glacier beds. *The Cryosphere*, *14*(12), 4495–4506. https://doi.org/10.5194/tc-14-4495-2020

Vasilyeva, M. A., Gusev, Y. A., Shtyrlin, V. G., Puzenko, A., Ishai, P. B., & Feldman, Y. (2014). Dielectric relaxation of water in clay minerals. *Clays and Clay Minerals*, *62*(1), 62–73. https://doi.org/10.1346/CCMN.2014.0620106

Weir, W. B. (1974). Automatic measurement of complex dielectric constant and permeability at microwave frequencies. *Proceedings of the IEEE*, *62*(1), 33–36. https://doi.org/10.1109/proc.1974.9382

Wersin, P., Curti, E., & Appelo, C. A. J. (2004). Modelling bentonite–water interactions at high solid/liquid ratios: Swelling and diffuse double layer effects. *Applied Clay Science*, *26*(1–4), 249–257. https://doi.org/10.1016/j.clay.2003.12.010